nature climate change

SUPPLEMENTARY INFORMATION
https://doi.org/10.1038/s41558-019-0602-x

In the format provided by the authors and unedited.

The effect of plant physiological responses to rising CO_2 on global streamflow

Megan D. Fowler[1*], Gabriel J. Kooperman[2], James T. Randerson[1] and Michael S. Pritchard[1]

[1]Department of Earth System Science, University of California Irvine, Irvine, CA, USA. [2]Department of Geography, University of Georgia Athens, Athens, GA, USA. *e-mail: mdfowler@uci.edu

The effect of plant-physiological responses to rising CO_2 on global streamflow

Megan D Fowler[1*], Gabriel J. Kooperman[2], James T. Randerson[1], and Michael S. Pritchard[1]

[1]Department of Earth System Science, University of California Irvine
[2]Department of Geography, University of Georgia Athens

Table of Contents

Supplementary Note

Evapotranspiration and vegetation response

Changes in the three components of evapotranspiration (ET) and leaf area index (LAI) are presented in *Figure S3*. As expected, the largest ET change in the *PHYS* simulations occur through decreased transpiration as a result of reduced stomatal openings in response to higher CO_2 concentrations[1,2]. *RAD*-driven changes in transpiration are also large, increasing throughout much of the world as rising temperatures increase atmospheric moisture demand; rising ground evaporation rates are present in this experiment as well, leading to overall large increases in ET at northern latitudes in *FULL (Supplementary Fig. S6*). Tropical reductions in *FULL* ET are instead primarily driven by *PHYS* transpiration changes, despite increased LAI in that simulation which would typically resist such a reduction.

These patterns agree well with the findings of past studies that have assessed the ability of *PHYS* and *RAD* to alter ET and LAI. *Skinner et al*. (2017)[3] note the strong effect of physiological forcings in the tropics, which lead to decreased ET via transpiration reductions and ultimately alter local precipitation patterns in heavily forested regions. These changes are also in line with the multi-model response of ET presented in *Figure S2* of *Swann et al.* (2016)[4] – *FULL* decreases in ET over parts of the tropics are primarily a result of *PHYS*, while northern latitude increases are *RAD*-driven instead. Those changes occur despite increases in LAI in both *PHYS* and *FULL* for each of the 7 models assessed. The agreement between past studies and the changes simulated here lends confidence to the validity of the hydrological forcing that will be assessed in the main text.

Environmental drivers of flood increases

We assess changes in key flood-related variables to identify the primary cause of increased flood frequency for each domain outlined in *Figure 1a*, focusing just on time-mean state variables during peak flood season. Since flood seasonality is regionally variable, we first define regional calendar month boundaries that straddle the 30-year composite seasonal cycle's annual interval of maximum discharge. For multiply stressed regions, the period of interest in the Southeast US is defined as Mar-Aug (inclusive), Jun-Oct in Southeast Asia, and Dec-Apr in Central Australia. In the *PHYS*-driven regions, this is defined as Dec-Jun in the Western Amazon, May-Nov in Central Africa, and Nov-May in Southeast Australia. Lastly, for the two *RAD*-driven regions, we consider the period of Aug-Dec for the Horn of Africa, and Jun-Oct in the India/Middle East region.

Overall, for multiply stressed regions (*Supplementary Table S1*) the results of this process confirm our initial hypothesis that reduced stomatal conductance in *PHYS* leads to increased flooding by enhancing antecedent soil moisture conditions. When only the land surface is able to respond to higher CO_2 concentrations in *PHYS* (left column), precipitation changes are small and not significant in any region. Soil moisture, however, increases significantly in all regions, as expected when the water use efficiency of plants rises. Tellingly, this occurs despite a lack of detectable change in shortwave radiation and resistive increases in productivity (represented here by gross primary productivity, GPP), which responds to elevated CO_2 in ways that would tend to dry the soil rather than moisten it. In contrast, when only the atmosphere is allowed to respond to enhanced CO_2 (*RAD*; middle column of *Supplementary Table S1*), precipitation increases in all three multiply stressed regions while other potentially important factors like snowmelt cannot explain the flood increase (i.e. statistically insignificant decreases in all regions). This increase of precipitation in the absence of other explanatory factors is also the case for regions that are driven almost exclusively by the *RAD* response, summarized in *Supplementary Table S2*. In regions that are primarily *PHYS*-driven in the *FULL* experiment, increased soil moisture is again found to be important, as was the case in multiply-stressed regions; however, in this case increases in precipitation over Western Amazon and Central Africa also contribute (*Supplementary Table S3; right column*) by rearranging precipitation patterns non-locally to these domains.

Annual streamflow validation

To assess the ability of CESM to capture reasonable streamflow responses to 4xCO_2, we compare the changes simulated in *FULL* to CMIP5 mean changes simulated in *Figure 1* of *K14*. The agreement in sign between the two datasets discussed in the main text is encouraging despite some regional and quantitative differences (*Supplementary Fig. S5*). In both cases, the two also agree on the general spatial pattern of changes to be expected. In general, Q_{peak} increases over much of the globe, but key exceptions to that occur in high-latitude western Europe and western North America (*Supplementary Fig. S4*). In these regions, strong polar-amplified warming in *RAD* reduces peak snowmelt rates to contribute to earlier and lower peak discharge during spring (*Supplementary Fig. S6*), consistent with increases in the ratio of precipitation falling as rain rather than snow (*Fig. 3*). In the Eastern Amazon region, declines are again linked to reduced mean precipitation[3,5–7] (*Supplementary Fig. S4*). Increases in Q_{low} in both *K14* and *FULL* are largest at northern latitudes, again due to increases in high latitude mean precipitation and the fraction falling as rain (*Supplementary Fig. S6; Fig. 3*). This result fits well with a general understanding of the drivers that control peak and low flows regionally; at high latitudes, Q_{peak} is often related to snowmelt, which is heavily influenced by *RAD* but very little by *PHYS*, which instead plays a larger role in the heavily vegetated and sunlit tropics. Responses for Q_{mean} were found to be quantitatively weaker but qualitatively similar to Q_{peak} (*Supplementary Fig. 4)*.

Annual streamflow cycles in the Amazon, Parana, Congo, and Yangtze

Despite obvious disagreements between the streamflow simulated in our pre-industrial *CTRL* and 1970-2005 observed river discharge (colored vs. dashed lines in *Fig. 5*), there is little reason to expect good agreement in experiments such as these. Both *CTRL* and *FULL* suffer from regional precipitation biases, including an Amazon dry bias, typical of most ESMs[8–11]. Precipitation in that basin is 27-39% lower than observed during the period of peak streamflow (*Supplementary Fig. S9)*, consistent with the underestimation of Amazon streamflow (*Fig. 5a*). Too much precipitation falls over the Congo during most months (*Supplementary Fig. S9*), consistent with streamflow overestimation there (*Fig. 5c*). Additionally, CaMa does not account for human management of river systems, which may cause disagreement in the Parana, which has a number of large dams[12] that may damp its seasonal amplitude. Nevertheless, despite these strongly varying bias structures in each basin, the effect of *PHYS* is consistent – the plant response to rising CO_2 drives increases in streamflow that dominate decreases or negligible changes in *RAD* in all four basins.

Supplementary References

1. De Kauwe, M. G. *et al.* Forest water use and water use efficiency at elevated CO_2: a model-data intercomparison at two contrasting temperate forest FACE sites. *Glob. Chang. Biol.* **19**, 1759–1779 (2013).
2. Ainsworth, E. A. & Long, S. P. What have we learned from 15 years of free-air CO_2 enrichment (FACE)? A meta-analytic review of the responses of photosynthesis, canopy properties and plant production to rising CO_2. *New Phytol.* **165**, 351–372 (2004).
3. Skinner, C. B., Poulsen, C. J., Chadwick, R., Diffenbaugh, N. S. & Fiorella, R. P. The role of plant CO_2 physiological forcing in shaping future daily-scale precipitation. *J. Clim.* **30**, 2319–2340 (2017).
4. Swann, A. L. S., Hoffman, F. M., Koven, C. D. & Randerson, J. T. Plant responses to increasing CO_2 reduce estimates of climate impacts on drought severity. *PNAS* **113**, 10019–10024 (2016).
5. Kooperman, G. J. *et al.* Forest response to rising CO_2 drives zonally asymmetric rainfall change over tropical land. *Nat. Clim. Chang.* **8**, 434–440 (2018).
6. Richardson, T. B. *et al.* Carbon dioxide physiological forcing dominates projected Eastern Amazonian drying. *Geophys. Res. Lett.* **45**, (2018).
7. Langenbrunner, B., Pritchard, M. S., Kooperman, G. J. & Randerson, J. T. Why does Amazon precipitation decrease when tropical forests respond to increasing CO2? *Earth's Futur.* **7**, 450–468 (2019).
8. Mehran, A., AghaKouchak, A. & Phillips, T. J. Evaluation of CMIP5 continental precipitation simulations relative to satellite-based gauge-adjusted observations. *J. Geophys. Res. Atmos.* **119**, 1695–1707 (2014).
9. Yin, L., Fu, R., Shevliakova, E. & Dickinson, R. E. How well can CMIP5 simulate precipitation and its controlling processes over tropical South America? *Clim. Dyn.* **41**, 3127–3143 (2013).
10. Sakaguchi, K., Leung, L. R., Burleyson, C. D., Xiao, H. & Wan, H. Role of troposphere-convection-land coupling in the Southwestern Amazon precipitation bias of the Community Earth System Model Version 1 (CESM1). *J. Geophys. Res. Atmos.* **123**, 8374–8399 (2018).
11. Lintner, B. R. *et al.* Relationships among climatological vertical moisture structure, column water vapor, and precipitation over the central Amazon in observations and CMIP5 models. *Geophys. Res. Lett.* **44**, 1981–1989 (2017).
12. FAO. La Plata Basin. *AQUASTAT Main Database, Food and Agriculture Organization of the United Nations (FAO)* (2016). Available at: http://www.fao.org/nr/water/aquastat/basins/la-plata/index.stm.

Supplementary Figures

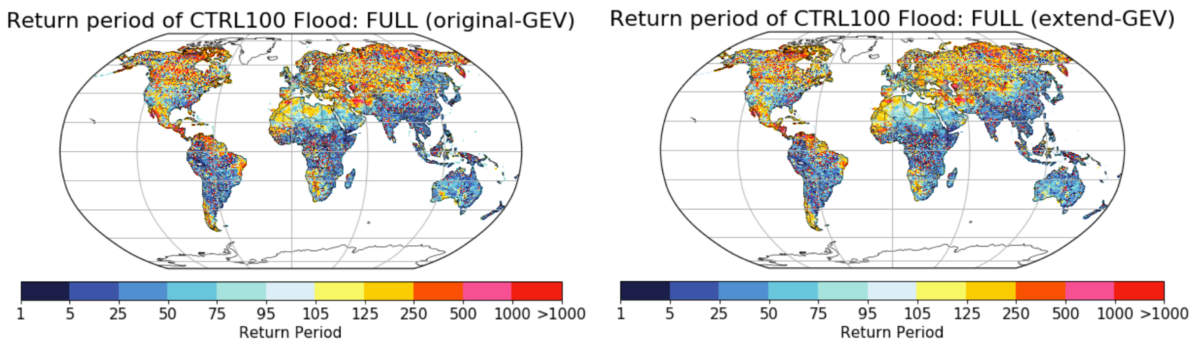

Supplementary Figure S1: Comparison of the FULL flood return period created from (left) the original 30-year period used for analysis and (right) the full 50-year sample wherein CO_2 is still held steady at four times its pre-industrial amount.

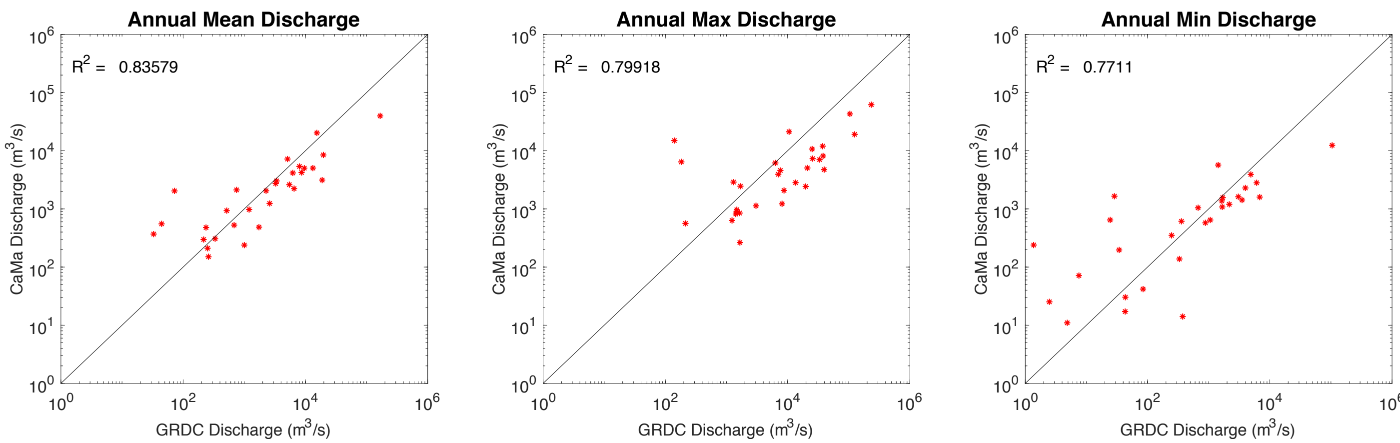

Supplementary Figure S2: Validation of CaMa-simulated time-mean and annual extremum statistics as downscaled from CESM runoff in CTRL against observed GRDC streamflow across a selection of large river basins.

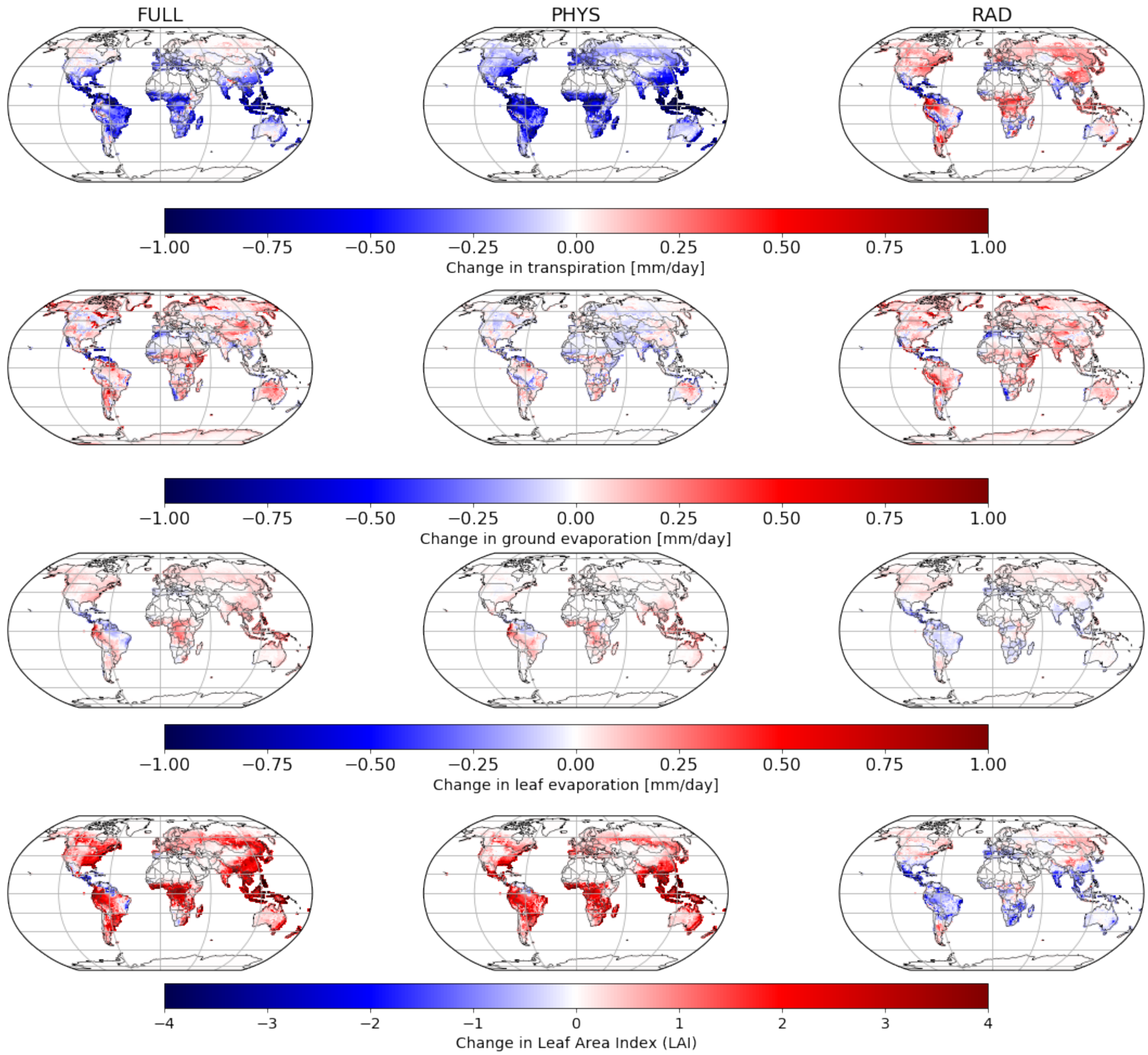

Supplementary Figure S3: Changes (relative to* CTRL*) in transpiration, ground evaporation, leaf evaporation, and leaf area index.

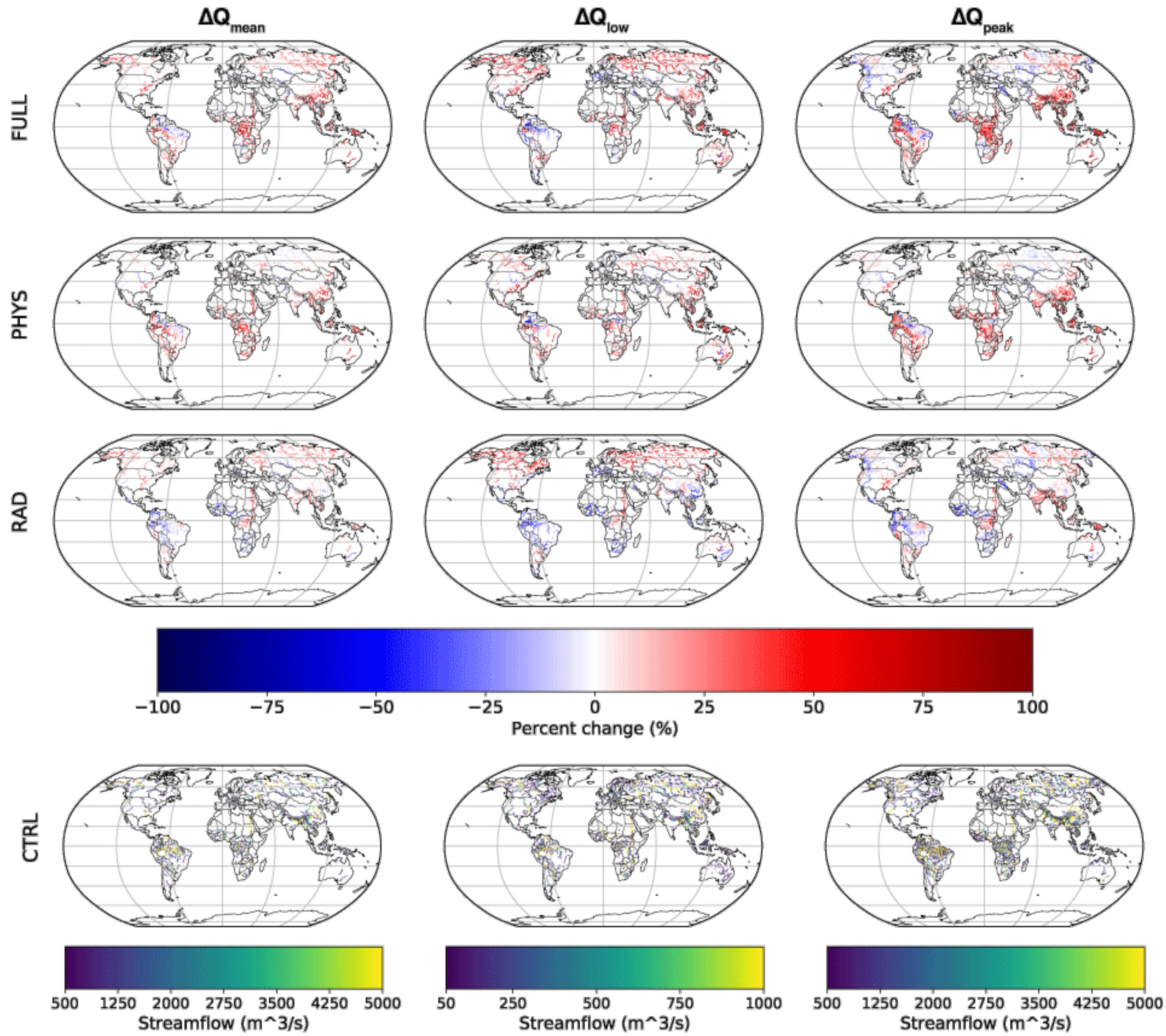

Supplementary Figure S4: Changes in annual mean streamflow (left), low streamflow (center), and peak streamflow (right) for **FULL, PHYS,** ***and*** **RAD** ***experiments. Background streamflow from*** **CTRL** ***is shown in the bottom panel. Masking is applied as in*** **Figure 2.**

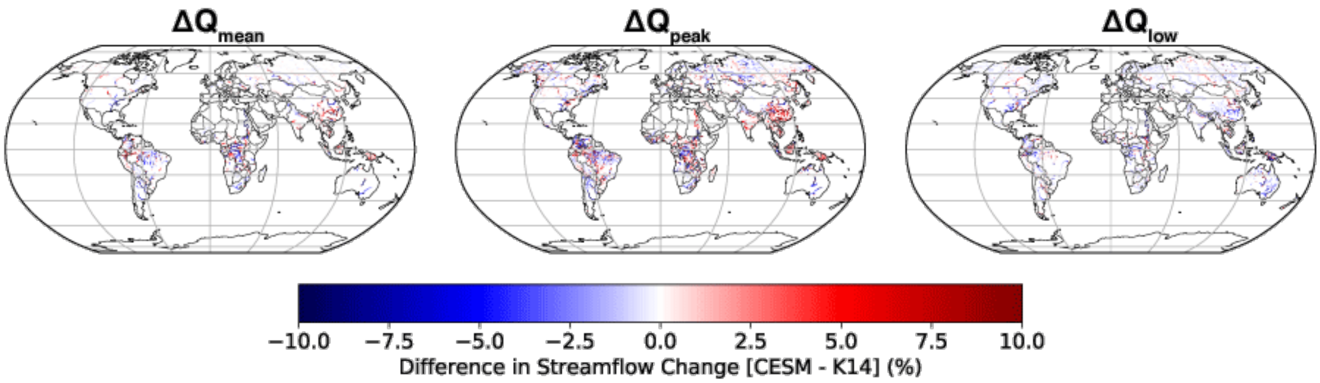

***Supplementary Figure S5:** Percent difference between the streamflow change in the CESM* FULL *simulation and the CMIP5 RCP8.5 multi-model means in* K14. *Note that the color bar here is ten times smaller than that of Figure S4.*

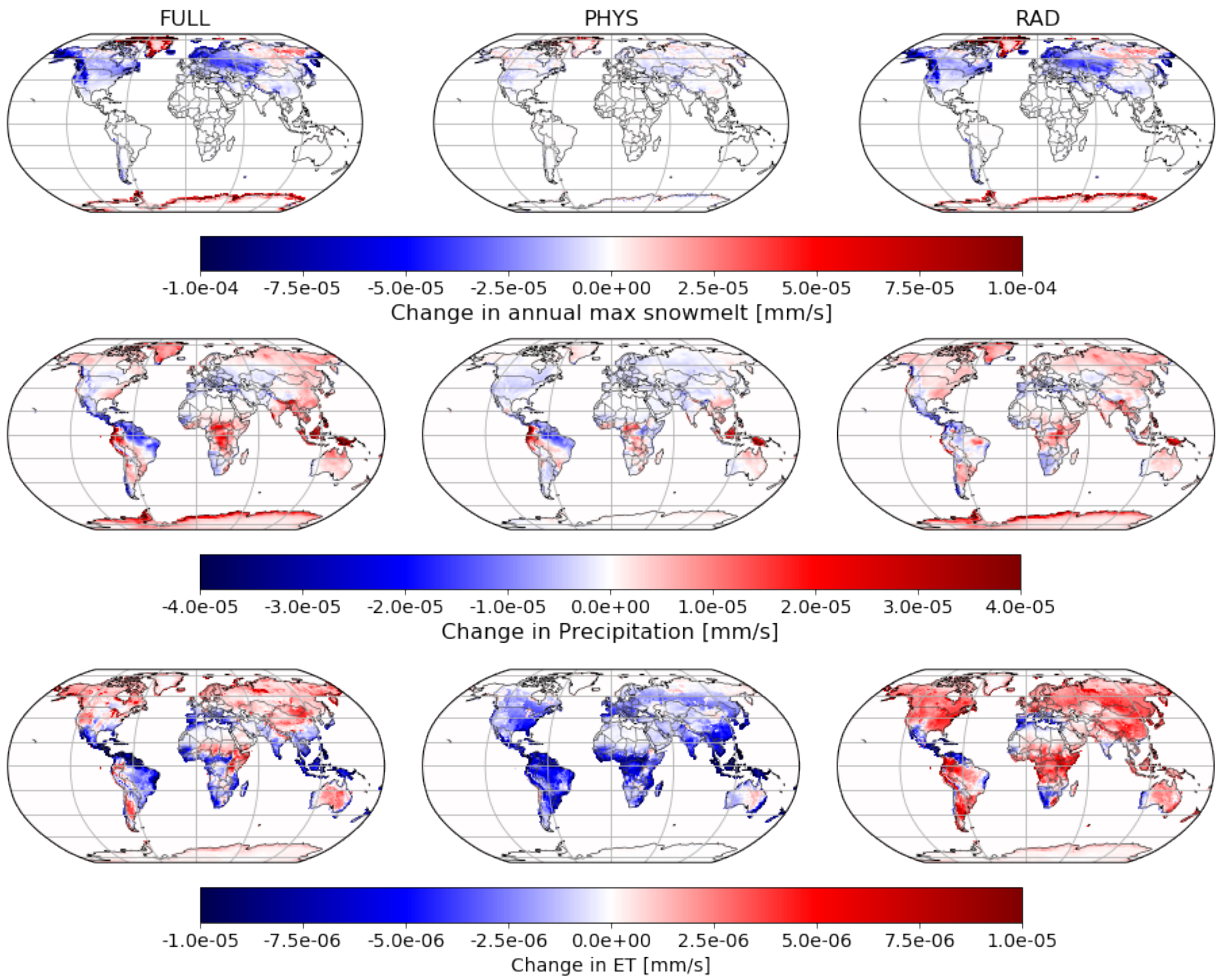

Supplementary Figure S6: From top to bottom: changes in annual maximum snowmelt rates, average precipitation rate, and average evapotranspiration in* FULL *(left),* PHYS *(center) and* RAD *(right) experiments.

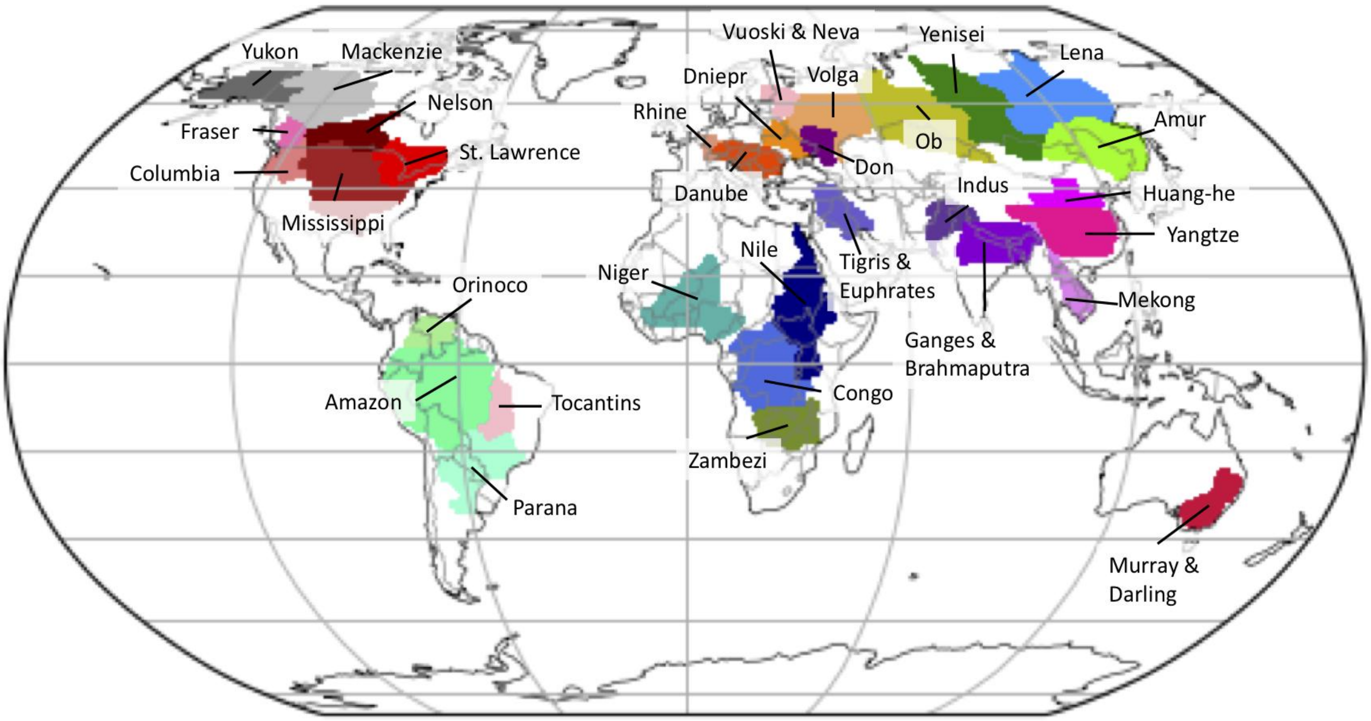

Supplementary Figure S7: River basins assessed in this study.

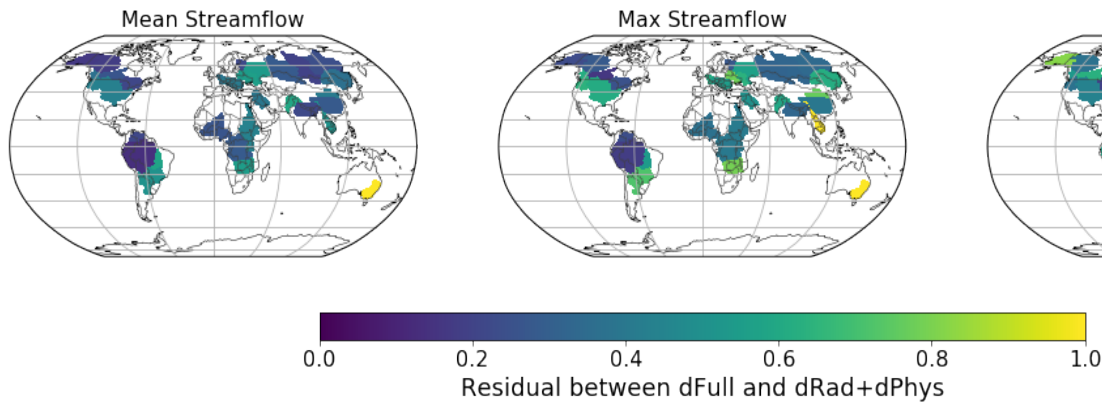

Supplementary Figure S8: Residual of linear equation, defined as the root mean squared error between FULL and RAD+PHYS for all 30 years in each basin.

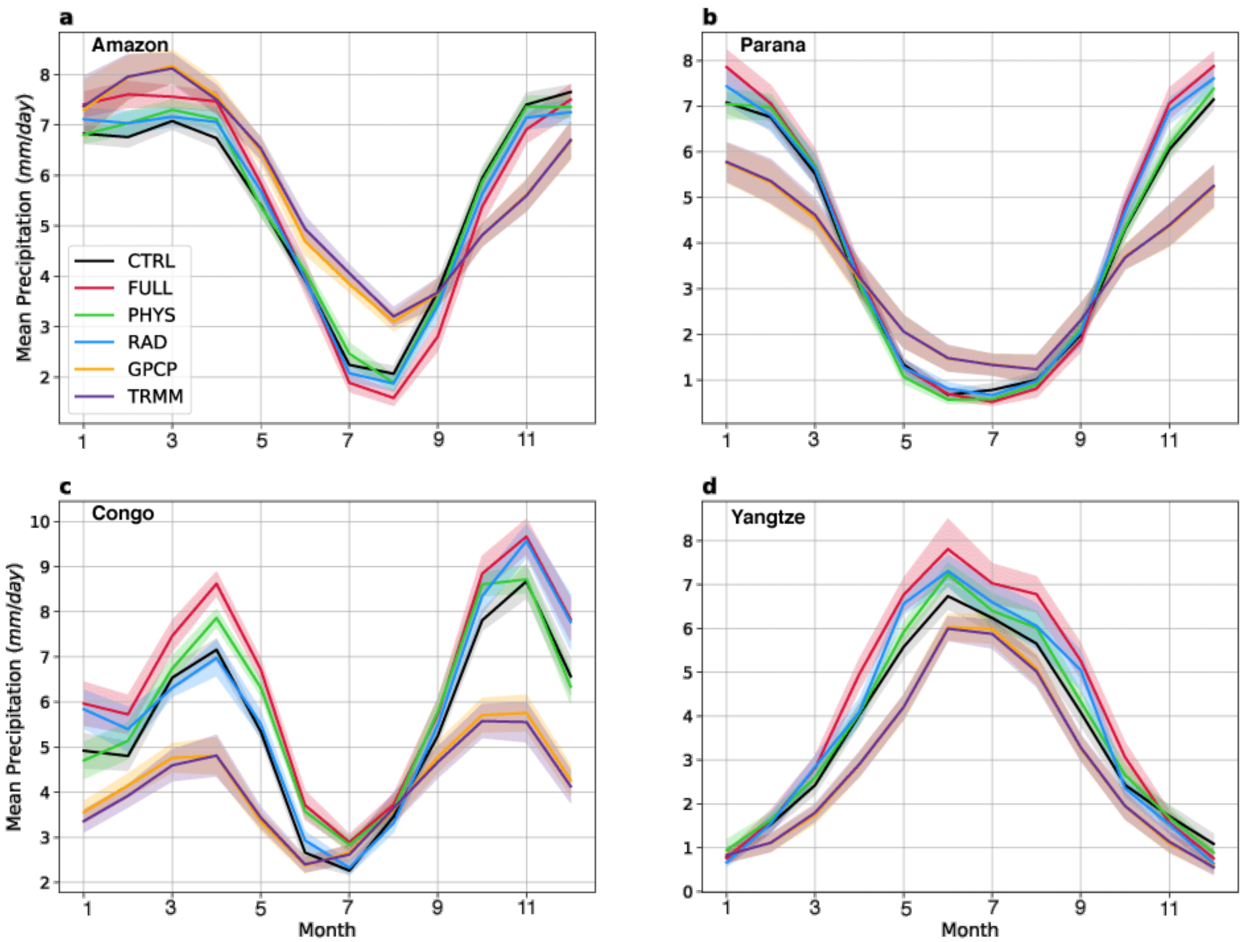

Supplementary Figure S9: Annual cycle of precipitation in basins selected for further analysis in **Figure 5*****. Observations are averaged from GPCP or TRMM over the period of 1998-2013, while CESM experiments are averaged over the 30-year period used for analysis. Both are averaged over the whole basin.***

Supplementary Tables

Multiply-stressed Regions									
	PHYS – CTRL			*RAD – CTRL*			*FULL – CTRL*		
	SE U.S.	**SE Asia**	**C. Aus**	**SE U.S.**	**SE Asia**	**C. Aus**	**SE U.S.**	**SE Asia**	**C. Aus**
Rain	-2.59	7.53	10.88	18.76	25.30	21.60	10.68	26.38	22.43
1m Soil Moisture	9.34	5.03	6.00	4.07	2.07	2.03	9.09	4.81	5.91
GPP	51.79	26.38	33.85	4.97	4.28	10.74	69.71	40.45	50.96
Surface Shortwave Radiation	2.18	1.17	-0.04	-2.78	-2.90	-1.04	-0.28	-1.29	-0.82
Snowmelt	73.32	-83.91	0.20	-90.70	-75.44	-16.09	-90.70	-75.44	-16.09
Runoff	104.89	78.42	65.74	92.85	82.32	68.89	132.68	110.49	109.89
ET	-13.80	-15.09	0.58	8.15	5.43	12.11	-4.23	-4.90	8.97
$CTRL_{100}$ Return Period	21.33	22.88	28.78	23.41	21.40	21.45	17.66	17.22	20.14

Table S1: (Top rows) Percent change in horizontally averaged climatological values of flood relevant state variables within the multiply stressed regions from Fig. 1 during their peak flood season (see text); (Bottom) return period of the $CTRL_{100}$ flood for the same regions. Values in black indicate significance at the 95% level (red values are not significant). Flood season is Mar-Aug for the SE U.S., Jun-Oct for SE Asia, and Dec.-Apr for Central Australia.

RAD-driven Regions						
	PHYS – CTRL		*RAD – CTRL*		*FULL – CTRL*	
	India	**Horn of Africa**	**India**	**Horn of Africa**	**India**	**Hon of Africa**
Rain	1.29	-5.85	18.64	25.56	20.18	23.57
1m Soil Moisture	1.18	0.11	1.72	5.91	2.34	7.86
GPP	29.81	19.76	-2.92	11.73	43.18	41.96
Surface Shortwave radiation	1.00	4.13	-1.51	-4.78	-1.54	-2.13
Snowmelt	-29.25	3.78	-81.54	-7.58	-81.54	-7.58
Runoff	19.42	29.33	31.95	43.87	52.10	76.16
ET	-11.26	-11.49	3.89	15.85	-5.03	7.73
$CTRL_{100}$ Return Period	249.87	337.48	24.42	15.53	23.20	16.87

Table S2: As in Table S1, but for RAD-driven regions. In these regions, the RAD-CTRL column is thus expected to show larger changes than the PHYS-CTRL one. Flood season is defined as Jun-Oct for India and Aug-Dec for the Horn of Africa.

PHYS-driven Regions									
	PHYS – CTRL			*RAD – CTRL*			*FULL – CTRL*		
	W Amazon	**C. Africa**	**SE Aus.**	**W Amazon**	**C. Africa**	**SE Aus.**	**W Amazon**	**C. Africa**	**SE Aus.**
Rain	12.28	12.70	5.32	-1.15	-1.27	11.91	16.45	21.08	12.16
1m Soil Moisture	10.06	9.43	12.25	-4.60	-4.84	-2.90	7.13	9.41	6.22
GPP	27.54	19.21	56.34	-2.79	9.56	2.54	49.10	34.10	63.79
Surface Shortwave radiation	3.20	1.05	0.89	3.79	-2.74	-0.14	5.38	-3.19	1.39
Snowmelt	11.76	10.53	-6.32	11.02	-49.55	-26.86	11.02	-49.55	-26.86
Runoff	81.29	130.41	152.76	-24.80	-31.40	-14.94	50.03	131.26	74.59
ET	-9.13	-16.65	-2.96	8.21	7.12	8.81	2.81	-8.23	6.21
$CTRL_{100}$ Return Period	6.97	16.16	15.83	342.26	348.13	303.39	8.15	11.62	20.71

Table S3: As in Table S1, but for PHYS-driven regions. In these regions, the PHYS-CTRL column is thus expected to show larger changes than the RAD-CTRL one. Flood season is defined as Dec-Jun for W Amazon, May-Nov for Central Africa, and Nov-May for SE Australia.

	Tropics (30˚S-30˚N)	**Mid- and high-latitudes (30-90˚S, 30-90˚N)**
PHYS	0.67	0.48
RAD	0.36	0.81

Table S4: Correlation coefficient (R) between the change in FULL and either PHYS or RAD (as depicted in Figures 2 and S3).

Q_{mean} *Linearity Analysis*

	$CTRL\ (m^3\ s^{-1})$	$\Delta FULL$ **(%)**	$\Delta PHYS$ **(%)**	ΔRAD **(%)**	ε (%)
Yukon	4011.96	33.68	2.66	29.81	16.61
Mackenzie	3700.77	29.09	10.69	19.66	17.91
Columbia	3144.51	14.65	3.87	23.02	43.46
Nelson	1175.45	15.06	8.82	18.65	26.32
Mississippi	2752.70	41.25	13.55	29.83	43.01
St. Lawrence	3426.80	7.05	-5.77	14.86	21.10
Rhine	1677.32	-0.81	8.91	-5.89	38.46
Danube	2290.04	-16.58	13.04	-22.88	41.17
Dniepr	1901.25	-4.89	9.56	9.26	54.90
Volga	3353.25	32.00	26.70	36.54	54.51
Ob	3129.92	2.90	2.26	-5.95	28.45
Yenisei	3694.71	26.55	8.41	19.91	19.59
Lena	4262.81	35.38	4.18	26.60	23.86
Amur	3688.36	57.62	26.79	26.47	36.52
Orinoco	8033.61	-12.24	2.94	-9.77	21.52
Parana	4118.13	49.37	70.42	-4.22	50.73
Amazonas	8584.14	14.45	31.74	-12.47	13.57
Niger	2604.15	19.46	50.63	-43.34	26.41
Congo	7722.23	63.93	42.69	9.04	28.50
Nile	5523.38	120.02	47.85	56.14	43.93
Zambezi	4101.12	32.39	48.97	-10.82	55.30
Tigris & Euphrates	958.72	-53.87	-4.32	-42.38	39.84
Indus	2897.65	-5.23	-3.27	-2.95	59.63
Ganges & Brahmaputra	5499.62	30.01	7.27	16.72	22.08
Mekong	3200.94	89.40	77.07	29.96	51.74
Huang-He	4207.62	32.31	12.93	12.78	41.08
Yangtze	5290.31	44.78	34.46	3.17	27.82
Murray & Darling	1430.79	105.39	197.73	-27.12	346.65
Don	2512.12	16.32	20.10	24.47	56.07
Fraser	2576.83	18.58	4.75	21.08	36.82
Tocantins	5144.31	-1.22	11.97	2.73	58.57
Vuoski & Neva	1039.55	22.35	-5.01	24.12	22.09

Table S5: For each of the basins assessed, 30-year averaged mean streamflow (Q_{mean}) is reported along with the percent change from that in FULL, PHYS, and RAD. The RMSE (ε)

values between ∆FULL and ∆RAD+∆PHYS for all thirty years is also reported. Basins that do not meet the linearity criteria are shown in grey.

Q_{peak} *Linearity Analysis*

	$CTRL\ (m^3\ s^{-1})$	$\Delta Full$	$\Delta PHYS$	ΔRAD	ε
Yukon	7496.18	0.32	5.24	-3.64	22.69
Mackenzie	6251.49	5.67	11.93	-1.87	27.97
Columbia	8725.18	-3.53	10.70	4.70	64.31
Nelson	1628.75	-0.42	5.09	0.63	15.78
Mississippi	3822.31	58.57	23.57	49.11	61.19
St. Lawrence	3775.37	9.34	-4.71	14.27	25.31
Rhine	3005.07	16.87	21.09	8.50	61.35
Danube	2885.41	-13.76	18.04	-21.47	55.23
Dniepr	2654.52	-3.81	16.31	16.79	78.35
Volga	6502.04	11.41	22.36	11.91	56.87
Ob	5691.13	-10.65	1.17	-18.74	31.94
Yenisei	7223.18	16.73	-0.13	14.22	32.48
Lena	8749.14	21.72	-2.86	22.94	34.30
Amur	5176.19	77.75	29.83	40.37	61.95
Orinoco	15938.49	18.51	22.36	3.48	23.68
Parana	6428.74	61.88	85.30	-3.39	72.05
Amazonas	12878.61	24.57	35.33	-5.93	17.83
Niger	4665.74	24.43	56.11	-40.38	37.37
Congo	13601.92	52.92	27.01	14.53	40.24
Nile	6083.53	119.93	53.50	55.40	41.20
Zambezi	8013.36	53.63	71.40	-6.18	78.97
Tigris & Euphrates	1296.36	-55.51	-2.07	-46.36	50.40
Indus	5929.52	-7.09	-2.15	-5.94	59.45
Ganges & Brahmaputra	11961.83	37.53	11.79	22.61	33.18
Mekong	5928.97	141.76	111.98	66.02	120.81
Huang-He	6357.90	52.56	23.50	20.37	76.62
Yangtze	9842.45	46.04	34.14	5.66	39.53
Murray & Darling	2877.77	149.66	312.39	-22.06	600.03
Don	4574.01	4.68	17.47	7.88	63.70
Fraser	8037.87	-12.24	18.26	-12.88	61.95
Tocantins	15096.85	11.62	15.99	5.43	54.57
Vuoski & Neva	1173.58	28.35	-4.03	28.46	27.25

Table S6: As in Table S5, but for peak flow (Q_{high}).

Q_{low} Linearity Analysis

	$CTRL\ (m^3\ s^{-1})$	$\Delta Full$	$\Delta PHYS$	ΔRAD	ε
Yukon	1118.12	223.74	7.73	206.82	81.72
Mackenzie	1959.35	80.97	24.02	67.06	37.88
Columbia	719.92	-1.83	-0.36	3.85	37.68
Nelson	710.94	57.94	28.81	67.47	63.57
Mississippi	1636.28	24.25	4.11	8.81	43.77
St. Lawrence	3103.41	5.60	-6.71	14.97	19.92
Rhine	699.42	-13.15	12.49	-9.39	80.95
Danube	1608.07	-20.42	12.03	-24.43	36.91
Dniepr	1113.61	0.10	10.27	15.56	74.98
Volga	1502.64	52.55	39.72	73.51	95.26
Ob	857.89	97.17	22.66	75.39	74.48
Yenisei	1643.60	56.88	26.13	33.07	27.16
Lena	1301.99	29.28	11.43	19.04	21.05
Amur	1920.18	92.45	54.71	37.82	49.04
Orinoco	1077.24	-35.79	-33.07	-9.61	50.67
Parana	2430.49	59.57	73.05	-1.61	68.29
Amazonas	2847.29	-10.23	47.39	-25.18	57.75
Niger	1298.61	16.12	51.42	-46.66	30.79
Congo	2841.73	94.06	96.08	-1.18	38.81
Nile	5091.86	121.02	47.89	57.17	50.95
Zambezi	1569.89	12.28	38.98	-14.78	48.76
Tigris & Euphrates	724.03	-57.94	-4.44	-44.44	38.29
Indus	440.80	38.56	-2.82	31.98	89.62
Ganges & Brahmaputra	732.20	69.48	18.28	32.27	84.14
Mekong	1211.87	51.63	53.15	10.78	53.88
Huang-He	2754.64	13.29	2.86	7.48	18.64
Yangtze	2104.30	43.15	44.61	-2.53	37.13
Murray & Darling	716.70	55.45	103.34	-26.28	123.79
Don	1364.88	4.85	19.82	22.71	64.35
Fraser	604.16	-0.19	6.07	12.45	53.44
Tocantins	239.66	-6.02	56.71	-7.20	142.26
Vuoski & Neva	889.14	18.41	-5.68	21.77	19.56

Table S7: As in Table S5 but for low flow (Q_{low}).